

Characterization of shallow geology by high frequency seismic noise tomography.

M. Picozzi⁽¹⁾, S. Parolai⁽¹⁾, D. Bindi⁽²⁾ and A. Strollo^(1,3).

⁽¹⁾ *GeoForschungsZentrum Potsdam, Telegrafenberg, 14473 Potsdam, Germany*

⁽²⁾ *Istituto Nazionale di Geofisica e Vulcanologia, via Bassini 15, 20133 Milano, Italy*

⁽³⁾ *University of Potsdam, Karl-Liebknecht-Strasse 24, 14476, Potsdam, Germany*

SUMMARY

To study the applicability of the passive seismic interferometry technique to near surface geological studies, seismic noise recordings from a small scale 2D array of seismic stations were performed in the test site of Nauen (Germany). Rayleigh wave Green's functions were estimated for different frequencies. A tomographic inversion of the travel times estimated for each frequency from the Green's functions is then performed, allowing the laterally-varying 3D surface-wave velocity structure below the array to be retrieved at engineering-geotechnical scales. Furthermore, a 2D S-wave velocity cross section is obtained by combining 1D velocity structures derived from the inversion of the dispersion curves extracted at several points along a profile where other geophysical analyses were performed. It is shown that the cross section from passive seismic interferometry provides a clear image of the local structural heterogeneities, which are in excellent agreement with georadar and geoelectrical results. Such a findings indicate that the interferometry analysis of seismic noise is potentially of great interest for deriving the shallow 3D velocity structure in urban areas.

Key word: seismic noise, Green's functions, tomography, surface waves, cross-correlation, S-wave velocity

Abbreviated title: High frequency seismic noise tomography

Corresponding author:

Matteo Picozzi, GeoForschungsZentrum, D-14473, Potsdam, Germany

Phone: +49-331-2881285

FAX: +49-331-2881204

e-mail: picoz@gfz-potsdam.de

Introduction

Recent theoretical studies have shown that the cross-correlation of diffuse wavefields can provide an estimate of the Green's functions between receivers (Weaver & Lobkis, 2001, 2004; Snieder, 2004; Wapenaar, 2004; Wapenaar and Fokkema, 2006). Using coda waves of seismic events (Campillo & Paul, 2003) and long seismic noise sequences (Shapiro & Campillo, 2004) it was confirmed that it is possible to estimate the Rayleigh wave component of Green's functions between two stations by the cross-correlation of simultaneous recordings, a method now generally referred to as seismic interferometry. These results allowed the first attempts of surface wave tomography at regional scales (e.g. Shapiro & Campillo, 2004; Sabra *et al.*, 2005; Shapiro *et al.*, 2005; Gerstoft *et al.*, 2006; Yao *et al.*, 2006; Cho *et al.* 2007; Yang *et al.*, 2007; Lin *et al.*, 2007) using seismic noise recordings from broadband seismic networks. Generally, for these kinds of studies, waves at frequencies well below 1 Hz were used to image the crust and the upper-mantle structure. A comprehensive review of the seismic interferometry method can be found in Curtis *et al.* (2006).

The seismic noise interferometry can be applied also to frequencies greater than 1 Hz. Schuster (2001) and Schuster *et al.* (2004) showed the possibility to form an image of the subsurface using cross correlation of seismic responses from natural and man-made sources at the surface or in the subsurface. Furthermore, in the context of exploration geophysics, Bakulin & Calvert (2004, 2006) firstly proposed a practical application of seismic interferometry showing that it is possible to create a virtual source at a subsurface receiver location in a well in practice. Other recent applications in the high frequency range have been proposed by Dong *et al.*, 2006, and Halliday *et al.* 2007 for surface-wave isolation and removal in active surveys. Among several reasons that stimulated the application of the seismic noise interferometry to high frequencies, there is the possibility of applying this technique to a suburban setting (Halliday *et al.*, 2008), and then to exploit this approach for engineering seismology purposes. Such a kind of application requires the knowledge of the subsurface structure from few meters to few hundred of meters, and for this reason the interest is moved towards the high frequency range.

The application of the seismic noise interferometry to high frequencies is not a merely change of scale, since it involves important questions still under discussion within the research community. For example, the effects of the high spatial and temporal variability in the distribution of noise sources occurring at the high frequency range are still under investigation (Halliday & Curtis., 2008), as well as the relationship between the wavelength of interest and station inter-distances. Finally, also the role played by the attenuation in the sediments, typically much higher than within rocks, is under investigation (e.g. Halliday & Curtis, 2008).

Several authors (e.g., Chavez-Garcia & Luzon, 2005; Chavez-Garcia & Rodriguez, 2007; and Yokoi & Margaryan, 2008) showed, for a small scale experiment at a site with a homogeneous subsoil structure, the equivalence between the results obtained by cross-correlation in the time domain and the well known SPatial AutoCorrelation analysis (SPAC) method (Aki, 1957). However, it is worth noting that for non-homogeneous subsoil

conditions, the SPAC method suffers a severe drawback. That is, generally, such a method is used to retrieve the shallow soil structure below a small array of sensors by means of the inversion of surface wave dispersion curves extracted by seismic noise analysis. In particular, the inversion is performed under the assumption that the structure below the site is nearly 1D. Therefore, if the situation is more complicated (2D or 3D structure), then the SPAC method can only provide a biased estimate of the S-wave velocity structure. On the contrary, one can expect that, similarly to what is obtained over regional scales, local heterogeneities will affect the noise propagation between sensors, and hence can be retrieved by analysing the Green's function estimated by the cross-correlation of the signals recorded at two different stations. For this reason, passive seismic interferometry is also believed to be a valuable tool for studying complex structure and estimating surface wave tomography also for smaller spatial scales of investigation.

The experiment presented in this study aims to verify the suitability of the seismic interferometry for seismic engineering and microzonation purposes. We first evaluated the possibility of retrieving reliable and stable Green's functions within the limitations of time and instrumentation that bound standard engineering seismological experiment. For example, in urban microzonation studies, the number of deployed sensors is generally not larger than 20 and the acquisition time does not last more than a few hours. We apply the seismic interferometry technique to recordings from a 21-station array installed in the Nauen test site (Germany) (http://www.geophysik.tu-berlin.de/menue/testfeld_nauen/; Yaramanci *et al.*, 2002) for the estimation of surface wave Green's functions, showing that passive seismic interferometry is a valuable tool for the characterization of near-surface geology. In fact, the test site has the advantage that its underlying structure, down to a depth of about 30 m, is well known, since several previous geophysical and geological investigations have been carried out. Our data analysis also included tests to estimate the necessary length of recording time in order to obtain stable Green's functions for the frequency range of interest.

Second, the travel times estimated from the Green's functions analysis for different frequencies are inverted in order to derive, innovatively due to the frequency range investigated and the scale of the experiment, the laterally-varying 3D surface-wave velocity structure below the array. After having carried out reliability tests, the tomographic results are compared with those available from other techniques. The suitability and potential of seismic interferometry for investigating soil structure in urban areas (especially important for seismic hazard assessment), where other standard geophysical methods relying on the assumption that the structure below the site is nearly 1D might be not suitable, are then discussed.

Test site Nauen-Berlin

The Department of Applied Geophysics of the Technische Universität (TU) Berlin, together with the unit Geophysical Methods for the Management of Resources of the Federal Institute for Geosciences and Natural Resources (BGR), selected a test site in Nauen (Germany) (Figure 1a) as an ad-hoc test field for hydro-geophysical tests (http://www.geophysik.tu-berlin.de/menue/testfeld_nauen/; Yaramanci *et al.*, 2002).

The geology of the Nauen site is representative for large areas in northern Germany, being characterized by Quaternary sediments formed during the last glacial period (Weichsel), overlying Tertiary clays. In particular, in Nauen the Quaternary sediments are mainly fluvial sands bordered by glacial till (Yaramanci *et al.*, 2002).

Several studies were previously carried out at the Nauen site, such as georadar measurements, 2D and 1D geoelectric surveys (Figures 1b,c), 1D spectral induced polarization (SIP) analysis, reflection and refraction seismic profiles, and surface nuclear magnetic resonance (SNMR) investigations (see the previous referred internet page for more details). These studies have allowed the underlying structure to be retrieved in great detail, both in terms of the geometry of the formation interfaces and their geophysical characteristics. In particular, regarding the subsoil structure, DC geoelectric and GP radar measurements carried out along a profile in the northern part of the test site (Figures 1b,c) showed that the top of the glacial till layer (identified as a major discontinuity both in the georadar sections and the DC geoelectric results) rises from 18 m depth in the south-west to 3-5m depth in the northeast (Figures 1b,c). The P-wave velocity of the shallow sand layer is estimated to be about 400 m/s in the vadose zone (i.e. the 4000 Ωm layer in the DC geoelectric section, Figure 1b), and about 1400 m/s in the aquifer (i.e. the 290 Ωm layer, Figure 1b), while for the glacial till they reach 3000 m/s (Yaramanci *et al.*, 2002). However, the latter is considered by the authors themselves to be not reliable, because the refraction in glacial till was not clear enough. S-wave velocities have not yet been measured at the test site. Nevertheless, the lateral and vertical lithological changes from unconsolidated sediments to compact glacial deposits indicated by DC geoelectric, georadar, and seismic refraction studies (although uncertainties about the absolute body wave velocities in the glacial till exist) suggest the existence of a significant impedance contrast in the S-waves velocity structure of the site. This wealth of information makes the Nauen test site particularly suitable for testing the reliability of innovative geophysical methods. We, therefore, performed seismic noise measurements at the Nauen site to check the suitability of noise tomography to image the shallow geology structure.

Data acquisition

An array of 21, 3 component, seismological stations (Figure 1a) was deployed for a week (May 3 to May 10, 2007) at the Nauen test site for recording continuously environmental seismic noise. Eighteen 24-bit digitizers (EarthDataLogger, EDL) were connected to fifteen 3D SM-PE-6/B 4.5 Hz sensors, one Mark L-4C-3D 1 Hz, and two Güralp CMG-3ESPC

broadband sensors. Moreover, three 24 bit RefTek digitizers were equipped with 4.5 Hz sensors. Although the instrumental response of the used sensors is very different, all of them work optimally in the frequency range that is aimed to be investigated (from a few Hz on). The sampling rate was fixed to 500 samples/sec in order to have a sufficiently high resolution in the time domain for tomographic analysis, and the minimum interstation distance was fixed to 4.7 m. All stations were equipped with GPS timing. Sensors were installed in small drilled holes to obtain a good coupling between the instrument and soil, and were covered in order to reduce any interference caused by wind.

The distribution of the stations shown in Figure (1a) highlights that the array covers the 2D structure of the site. Moreover, in order to have a geometry of acquisition adequate for both the tomographic analysis and for minimizing bias effects in the analysis due to a non-uniform distribution of noise sources, stations are arranged in a way that a good azimuthal coverage, as well as a sufficient sampling of inter-sensors distances between the minimum (4.7 m) and the maximum (104.8 m), is obtained.

Correlation analysis

The continuous vertical noise recordings acquired at the Nauen test site were used to compute the cross-correlations between each pair of stations, that in turn were used to estimate the travel times of Rayleigh waves (e.g. Campillo & Paul, 2003; Shapiro & Campillo, 2004; Snieder & Safak, 2006; Mehta *et al.*, 2007). Since the aim of this work is to investigate the suitability of noise tomography as a tool for detecting lateral heterogeneities in S-wave velocity at depths less than a few tens of meters below a small scale array (maximum aperture of the array is of the order of about one hundred meters), only high frequencies (higher than a few Hz) are of interest. Therefore, a 2nd order Butterworth high-pass filter with a corner frequency of 0.9 Hz was applied to the noise recordings previously corrected for the instrumental response, in order to improve both the signal-to-noise ratio for the frequency range of interest (i.e. > 1 Hz), and to mitigate the influence of large-amplitude low-frequency signals in the cross-correlation functions. From the continuous data streams, 480 non-consecutive noise windows 30 s wide suitable for the frequency range of interest (Picozzi *et al.*, 2005) were extracted from different days and different hours, in order to take into account possible large temporal noise amplitude variations. Before computing the cross-correlations, the linear trend was removed from each window and a 5% cosine-taper was applied at both ends. After having tested several procedures proposed in the literature (Bensen *et al.*, 2007), the cross-correlations were computed considering one-bit normalized data (e.g. Campillo & Paul, 2003; Bensen *et al.*, 2007), that yielded the highest signal-to-noise ratio for the data set at hand. Finally, the time derivatives of the cross-correlation functions were estimated. Non-isotropic distribution of noise sources might lead to asymmetrical Green's functions when they are plotted against the inter-station distance. Therefore, in order to be able to detect such features, a geographical ordering was carried out before computing the cross-correlation, by always correlating the recording of the southernmost station of each pair with the northernmost one.

To estimate the group velocity at twelve different frequencies (i.e. 14 Hz, 12 Hz, 11 Hz, 10 Hz, 9 Hz, 8 Hz, 7.5 Hz, 7 Hz, 6.5 Hz, 6 Hz, 5.5 Hz, and 5 Hz), the cross-correlation functions were filtered by applying a Gaussian filter with a narrow band-width (Dziewonski *et al.*, 1969; Li *et al.*, 1996; Shapiro & Singh, 1999). Generally, the measured group velocity at each frequency provides information about the underlying velocity structure to a depth of about one-quarter wavelength of that frequency. Therefore, considering the S-wave velocity generally observed in literature for the soft sediments in Nauen, the selected frequency range is suitable for imaging the velocity structure from about 3 m down to about 30 m depth.

For each pair of stations, all estimated cross-correlations at the considered frequencies were stacked together to reduce the bias due to fluctuations in space of the noise sources (e.g. Pedersen *et al.*, 2007), with the resulting Green's functions normalized to a maximum amplitude of ± 1 . Finally, the propagation delay between the stations was estimated by picking the maximum on the Green's functions envelope, computed through a spline interpolation. The stability of the estimated Green's functions G was also investigated (Figure 2). For this purpose, the root mean square (RMS) difference between Green's functions obtained from increasing the number n of stacked cross-correlations, G_n and the G_{n-1} , was computed for frequencies 14 Hz and 6 Hz.

Figure (2) shows that, independent of the frequency, after stacking 50 cross-correlation functions, the RMS no longer significantly changes. This means that, using noise windows 30 s wide, about 20-30 minutes of signal is sufficient for obtaining an estimate of the Green's functions between the two sensors, suggesting the possibility of an application of this method to less favourable environments (like urban areas) where long instrumental installations would not be possible.

Several tests we performed using the vertical and also radial Green's functions, although not discussed in this paper, based on polarization analysis showed that the vertical component cross-correlation functions are dominated by Rayleigh waves. Figure (3a,b) shows an example of vertical and radial Green's functions calculated for the central frequency of 6 Hz. A clear elliptical particle motion is highlighted in the time window selected for the velocity estimation (Figure 3c).

Figures (4a) and (5a) show the computed Green's functions against distance for 14 and 6 Hz. These frequencies represent the upper and nearly the lower bound of the frequency range that was investigated. For frequencies lower than 5 Hz, the travel times estimated from the Green's functions were severely affected by random noise, which is probably related to Rayleigh wave group velocities too high to be detected with the available station interdistance. On the other hand, frequencies higher than 14 Hz were not investigated because these are related to only the first meter depths.

While the Green's functions at 6 Hz are almost symmetric (Figure 5a), those computed at 14 Hz show a stronger peak in the positive-time side (Figure 4a), suggesting directionality in the noise propagation. The frequency-wavenumber (f - k) analysis carried out using the Maximum Likelihood method (Capon *et al.*, 1967) shows that the distribution of the sources of seismic noise for the two frequencies is indeed different in the 2D-wavenumber plots (Figures 4b and 5b). In fact, at 6 Hz the sources are distributed homogeneously over all the azimuths, therefore generating symmetric Green's functions (Paul *et al.*, 2005; Stehly *et al.*, 2006;

Pedersen *et al.*, 2007). At 14 Hz the sources of seismic noise are more scattered over the wave-number plane, with the largest energy contribution coming from the southern and western directions. The asymmetry of the Green's functions (showing a more clear causal part) is consistent with the non-uniform distribution of seismic noise sources, as indicated by the f-k analysis (Figure 4b). The effect of the directionality of the high frequency noise on the estimated time delays was investigated by plotting the distribution of the travel times as a function of the distance and azimuth between each pair of stations. Figures (4c) and (5c) show that the travel time variations are dependent mainly on the inter-station distances, with travel times increasing, as expected, with increasing distance. No systematic variation of travel times with azimuth is shown. This indicates that the travel time estimate is stable even if the majority of sources are clustered in a narrow azimuthal range, provided that enough energy is coming from the remaining azimuthal sectors. This result is in agreement with Yang & Ritzwoller (2008) who reached similar conclusions after numerical simulations, and with the stationary phase analysis of Snieder (2004).

Surface wave tomography: the algorithm

The inter-station travel times estimated from the Green's functions were inverted by a tomographic approach in order to derive a 2D frequency-dependent Rayleigh wave velocity model. For media characterized by large velocity anomalies, the general ray theory inversion requires the implementation of nonlinear inversion techniques that take into account the wave-path and wave-curvature dependence on the structural model. However, considering the level of errors commonly hampering the input data for tomographic studies derived from shallow seismic surveys, a bias of a few percent in the estimated models due to the application of a simplified linear approach can be generally tolerated (Kugler *et al.*, 2007). Therefore, assuming that the velocity model varies smoothly over the distance of a wavelength, the analysis can be performed assuming the linear ray theory.

The tomographic inversion was performed for each frequency by dividing the investigated area into several constant group velocity cells and using the observed travel times to estimate the slowness (reciprocal of velocity) in each cell. The linear tomography problem of computing the integral travel time (t) for a given slowness (s) along a raypath is given by

$$t = \int s \cdot dl, \quad (1)$$

where the dl is the line element along the raypath. Equation (1) can also be expressed in a simple discrete matrix form,

$$\mathbf{t} = \mathbf{L}_1 \mathbf{s}. \quad (2)$$

In equation (2), \mathbf{t} is the vector of observed travel times, \mathbf{s} is the slowness of the cells, and \mathbf{L}_1 is an $M \times N$ matrix of ray-path segments, namely, M rays crossing the medium, divided into N cells.

Since our data inevitably contains errors and the considered problem is over-determined, equation (2) was solved in a generalized least-squares sense (e.g. Wiggins, 1972; Arai & Tokimatsu, 2004). Following Long & Kocaoglu (2001), we adopted an iterative procedure. The scheme was initialised by considering a homogeneous 2D model. The velocity of the

initial model was obtained by performing a linear fit between the observed travel times and the inter-station distances. Figure (6) shows the theoretical travel times obtained from the average Rayleigh wave slowness estimated for 14 Hz and 6 Hz. Outliers with respect to the average linear trend were removed to avoid biases in the following least squares inversion.

This average slowness was the initial guess $s^{(k=1)}$ for the iterative scheme. Then, a new solution $s^{(k+1)}$ was determined by solving the following equation

$$\mathbf{W}\Delta\mathbf{t}^{(k)} = \mathbf{L}_2\Delta\mathbf{s}^{(k)}, \quad (3)$$

in which $\Delta\mathbf{t}$ is the vector of the normalized misfit between the observed and theoretical travel times, $[\mathbf{t}_0 - \mathbf{t}_t] / \mathbf{t}_0$. Similarly, $\Delta\mathbf{s}$ is the vector of the normalized slowness modification $[\mathbf{s}^{(k)} - \mathbf{s}^{(k-1)}] / \mathbf{s}^{(k)}$. The diagonal matrix $\mathbf{W}_{(M \times M)}$ is made up of weighting factor elements defined by the adaptive bi-weight estimation method (Tukey, 1974), and was introduced to stabilize the iteration process (Arai & Tokimatsu, 2004).

The design matrix \mathbf{L}_2 in equation (3) is derived from \mathbf{L}_1 in equation (2), after that some proper modification was included to account for *a priori* constraints on the solution. In particular, it is expressed as

$$\mathbf{L}_2 = \begin{bmatrix} \mathbf{W}\mathbf{L}_1 \\ \mathbf{K}(\delta^2)\mathbf{M} \end{bmatrix}, \quad (4)$$

where the upper block is the ray-path segment matrix \mathbf{L}_1 properly weighted by the matrix \mathbf{W} , while, the damping coefficient δ^2 and the matrices \mathbf{K} and \mathbf{M} describe the *a priori* constraints imposed on the solution.

In particular, the matrix $\mathbf{K}_{(N \times N)}$ weights the data depending on the number, length, and orientation of each ray-path segment crossing each N_i cell. Following Kissinger (1988), each cell N_i is first divided into four quadrants. Then, the length of the rays passing through each sector is summed, resulting in a 2x2 ray density matrix. The ray density matrix was factorized by performing the singular value decomposition (SVD) (Golub & Reinsch, 1970). The singular values (λ_1, λ_2) were used to compute the ellipticity ($\lambda_{min}/\lambda_{MAX}$) of the ray density matrix. Since the case of rays randomly distributed over the azimuths corresponds to ellipticity close to 1, a good resolution for a given cell is achieved when the ellipticity is close to 1 and several rays cross the cell. Then, the elements of the matrix \mathbf{K} in equation (4) were computed by multiplying the ellipticity for the number of rays crossing each cell.

Matrix \mathbf{M} in Eq.(4) constrains the solution to vary smoothly over the 2D domain, and it was introduced to increase the stability of the inverse problem by reducing of the influence of travel time errors (Ammon & Vidale, 1993). The implementation of that smoothness constraint consists in adding a system of equations to the original travel time inversion problem,

$$s_{x,y} - \sum_{i=1}^R a_i s_{x-dx_i, y-dy_i} = 0, \quad (5)$$

where R is the number of cells surrounding the selected one, $s_{x,y}$, and a_i are the normalized weights (Figure, 7). Therefore, the slowness of each cell (i.e. showed using bold characters in the examples of Figure 7) composing the final image is related also to the slowness of the surrounding cells (i.e. showed in the same figure using italic characters), with weights depending on the cell's location.

It is worth noting that the matrix \mathbf{M} is not merely a low-pass filter in the classical sense, since the total amount of slowness fluctuation, and not individual contrasts, is limited (Ammon & Vidale, 1993).

Finally, the term δ^2 in equation (4) is a damping coefficient introduced to balance resolution and instability in the inversion analysis (Ammon & Vidale, 1993; Long & Kocaoglu, 2001). After some trial and error tests, δ^2 was fixed to 0.5.

Equation (3) was solved using the SVD method (e.g. Golub & Reinsch, 1970; Arai & Tokimatsu, 2004):

$$\Delta \mathbf{s}^{(k)} = \mathbf{V} \Lambda^\varepsilon \mathbf{U}^T \mathbf{W} \Delta \mathbf{t}^{(k)}, \quad (6)$$

where the factorization of \mathbf{L}_2 is $\mathbf{U} \mathbf{A} \mathbf{V}^T$ and the non-zero elements of the diagonal matrix Λ^ε are equal to $(\lambda_{ij} / (\lambda_{ij}^2 + \varepsilon^2))$, where λ_{ij} are the singular values of \mathbf{A} , and ε^2 is a damping factor (Long & Kocaoglu, 2001). After some trial-and-error tests, it was found that a value of $\varepsilon^2 = 0.5$ provides a satisfactory compromise between smoothness of solution and data misfit.

The slowness modifications in equation (6) were computed iteratively until a reasonable compromise between the reduction of the root mean square error between observations and predictions and the norm of the solution was achieved. Depending on the frequency value, the iterative process was stopped after a number of iterations varying from 50 for the higher frequencies to 200 for the lower ones.

Surface wave tomography: results, validation and error estimation

Results

The algorithm described in the previous section was used to determine a tomographic 2-D velocity model. Results are shown as velocities for the sake of similarity with standard surface wave 1D survey methods. The inversion procedure was repeated for the twelve selected frequencies for which the Green's functions were computed.

Resolution of images in surface-wave group-velocity tomography is regulated by wavelength and imaging methods (Long & Kocaoglu 2001). The quarter-wavelength limit criteria suggested that for the selected frequencies, an average resolution of 10 meters can be achieved. Hence, for sake of simplicity, the analysed area was divided into 10 X 10 m cells.

Other approaches using adaptive meshing depending on frequency can, of course, also be used.

Figure (8) shows the inversion results for the inter-station travel times estimated by the Green's functions at frequencies 14 Hz and 6 Hz. Group Rayleigh wave velocities are shown only for cells crossed by rays, and the few ones uncrossed by rays but influenced by the smoothing *a priori* constraints imposed on the solution. Considerable differences between the tomographic images appear at a first glance. The Rayleigh wave velocity for 14 Hz is almost constant (Figure 8a), suggesting that the medium is quite homogeneous down to the first 4-5 m depth. On the other hand, the tomographic image for 6 Hz (Figure 8b), shows an increase in Rayleigh velocity from the south-west sector of the explored area toward the north-east, suggesting the presence of a significant lateral contrast (i.e. velocities change from about 150 m/s to about 250 m/s) at depth between 10 m and 20 m, on the base of the observed velocities. The retrieved tomographic models allowed for a decreasing of the root mean square error of about 68% at 14 Hz and 55% at 6 Hz, with respect to the initial uniform velocity model.

Validation

In order to verify the capability of the ray-path geometry to resolve anomalous slowness distribution, tests with synthetic data were performed. Such tests allow us to better understand the combined influence on the solution stability of the damping parameter ε , the spatial-smoothing operator \mathbf{M} , the ray density matrix \mathbf{K} , and the number of performed iterations.

We perform validation tests using two different initial models (Figure 9a). In the first test a checkerboard model (Leveque *et al.*, 1993) with a side of about 50 meters was used. The input model for the second test resembled the structure of the velocity model expected for the Nauen test site. Thus, the synthetic model presented a lateral contrast between the south-west and north-east sectors of the same magnitude as the one supposed to be present in the Nauen field-test area between about 5 Hz and 7 Hz (Figure 9a).

The synthetic travel times were perturbed by adding random errors extracted from a normal distribution having zero mean and standard deviation equal to the standard deviation of the residual distribution between observed data and travel times predicted by the starting uniform velocity model at 6 Hz. In both tests with synthetic data, the average slowness of the synthetic velocity model was used as a starting guess.

The comparison between synthetic and restored models (Figure 9) shows that both the checkerboard structure and the simulated anomaly are satisfactorily reproduced. Since the central area of the synthetic model correspond to the region where the path coverage is denser, the lateral contrast in the restored image is less sharp due to the action of the applied smoothing constraints (matrices \mathbf{K} and \mathbf{M} of equation 4).

The results of the synthetic data inversion support the notion that the features obtained by inverting the empirical slowness are reliable. In particular, the general trend in the velocity path observed at higher depths (i.e. 6 Hz, Figure 8b) can be interpreted as being determined by an effective lateral variation of the soft-sediment mechanical properties.

The Bootstrap Analysis

Over the last few decades, modern statistical techniques such as Bootstrap or Jackknife (Efron & Gong, 1983) have been proposed to quantitatively determine the error bound for specific model parameters. Recently, computational power improvements have resulted in an increase in the use of such techniques in several fields of geophysics (e.g. Parolai *et al.*, 1997). Hence, here we propose the application of the Bootstrap technique to the tomographic problem presented in this work.

The Bootstrap method consists in repeated inversions (1000 times in our case) considering several datasets, called bootstrap samples, obtained by randomly sampling, with replacement, the set of observed travel times. Each bootstrap sample has the same size as the original dataset and the bootstrap estimate of the standard error is given by the standard deviation of the distribution of the reconstructed velocity models (called bootstrap replications) obtained for each bootstrap sample. Finally, the standard deviation for the velocity model obtained by the inversion of the original dataset is estimated from the values of the Bootstrap standard error and the number of data.

Figure (10) shows the standard deviation estimated for the tomographic models obtained for 14 Hz and 6 Hz. It is worth noting that, with the exception of only a few points, the standard deviation is smaller than 20 m/s, especially in the central part of the model where most of the stations lie. These results confirm the reliability of the estimated Rayleigh wave velocity distribution for depths between 15 and 20 m.

Depth Inversion and discussion

The last step of our analysis consists of determining the S-wave velocity over the vertical section selected in correspondence of the DC geoelectric and GP radar profiles (Figure 1).

Differences between Rayleigh wave phase and group velocities are very small when the latter are measured in the high frequency range (5-14 Hz) from very narrow-band filtered Green's functions, as in the procedure described in the previous part of this study. In order to verify this point, Rayleigh phase velocities were estimated from the estimated Green's functions by applying the Complex trace Analysis of Surface Wave method proposed by Parolai (2008) adapted for this case. The method simply estimates the phase velocity using a couple of Green's functions at a time by means of computing their Hilbert transform and their instant phases. Similar results have also been obtained by applying the technique proposed by Yao *et al.*, (2006). Analysis of the instantaneous Rayleigh phase velocity distribution for some frequencies (not shown here) indicated that differences observed between these values and the retrieved group velocities were smaller than their associated level of uncertainty.

For this reason, we perform the inversions for the S-wave velocity model estimation considering the observed velocities in the 2D frequency dependent tomography as representative of Rayleigh wave phase velocities. Therefore, following Brenguier *et al.* (2007), we determined the Rayleigh wave velocity dispersion curves (i.e. using all the available frequencies) for each cell along the profile (ten cells in our case) where the other geophysical surveys were performed. The obtained dispersion curves were then inverted using

a procedure similar to Parolai *et al.* (2006), based on the use of genetic algorithm (Yamanaka & Ishida, 1996). Finally, a vertical 2D S-wave velocity model was derived by interpolating, with a standard Kriging algorithm (Davis, 2002), the ten 1D S-wave velocity profiles (Figure 11).

The most interesting feature shown by the S-wave velocity section is the trend of the impedance contrast between low and high velocity sediments. In fact, moving from the south-west side of the section towards the northeast, the total thickness of the soft, low velocity layer decreases from about 20 meters to 10 meters. Since independent estimations of the S-wave velocity are not available, the reliability of the absolute velocity values cannot be checked. However, the outline of the general structure for the area provided by the other geophysical surveys (see Figure 1) are in good agreement with the one estimated from the approach proposed in this work (Figure 11). Namely, the level which is identified in the DC geoelectric and GP radar sections to be the glacial till very well corresponds both in absolute depth and in the general trend with the high impedance contrast level identified in our 2D S-wave velocity section.

In conclusion, comparing our results with those of other geophysical techniques and the derived geological model give us confidence in the capability of the proposed method to provide a reliable estimate of the shallow 3D Rayleigh and S-wave velocity model of an area. Finally, we add some additional comments about the role played by the surface-waves higher modes in both interferometric analysis and tomographic studies. The seminal works of Tokimatsu *et al.* (1992) and Tokimatsu (1997) showed that, at the engineering-geotechnical scale, the energy amount associated with higher modes depends on both the source distribution and the S-wave velocity structure. In particular, higher or multiple modes might play a significant role over some frequency ranges, when the S-wave velocity of the ground varies irregularly with depth (i.e. inversely dispersive). Furthermore, these authors demonstrated that the dispersion curve might also vary with the source-to-receiver distance. Hence, the phase velocities have to be considered a local quantity and their values depend on the location where the dispersion curve is evaluated (Lai, 1998). As a consequence of this behavior, the dispersion curve of Rayleigh waves is named the effective or apparent curve.

In agreement with the previous findings, the formulation proposed by Tokimatsu *et al.* (2002) for the computation of surface-wave phase velocities, that take into account the presence of higher modes, is commonly used in homogeneous subsoil conditions (e.g. Parolai *et al.*, 2005; Picozzi *et al.*, 2005; Parolai *et al.*, 2006; Picozzi & Abarello, 2007; Picozzi *et al.*, 2007). In order to discriminate the presence of higher modes and to evaluate their influence, the FK analysis proposed by Capon (1969) for 2D array of sensors can be used.

In a recent study (Halliday & Curtis, 2008) showed that, depending on the seismic sources distribution, higher modes might not be correctly estimated with the classical interferometry analysis. For the investigated site Figures (4b) and (5b) show that the energy associated with higher modes is negligible, in agreement with the quite simple and normal dispersive S wave velocity profile. Thus, the seismic noise wave-field we recorded is dominated, over the whole frequency range of interest, by the fundamental mode of the Rayleigh wave and the bias on the estimated Green's function due to higher modes is negligible. However, such findings should be taken into account when high frequency tomographic or geophysical exploration

studies (e.g. Bakulin & Calvert 2004, 2006; Draganov et al., 2007; Metha et al., 2007) are performed by applying the seismic interferometry approach. In fact, being seldom the availability of densely sampled array, the missing of a correct discrimination of the energy associated to all higher mode surface waves might lead to significant biases in the results.

Conclusions

In this study we report on the innovative application of seismic interferometry to high frequency seismic noise recordings (vertical component) for investigating the 3D shallow structure (15-20 m) at the Nauen test site.

First, we evaluated the possibility of retrieving reliable and stable Green's functions within the limitations of time and instrumentation that bound standard engineering seismology experiments. We showed that reliable Green's functions for the frequency range investigated (5-14 Hz) can be obtained with just 30 minutes of recordings. This result, together with the observation that a non-uniform distribution of noise sources does not preclude robust travel time estimates, encourages the use of the proposed technique as an exploration tool in urban areas.

We showed that with a limited (21) number of seismological stations, a 2D model of the subsoil structure can be obtained in the form of group velocity maps of Rayleigh waves for different frequencies. We estimated the reliability of the results through synthetic tests and bootstrap analysis, showing that a satisfactory resolution is achieved and that results are well constrained.

The dispersion curves for several points along the profile, for which independent geophysical results (georadar and geoelectric) are available, were extracted and inverted. Combining the 1D velocity structures below each site, a 2D S-wave velocity cross section was derived. The excellent agreement in the position of the main geological/geophysical boundary along the cross section with the georadar and geoelectrical investigation results highlight the potential of the method for deriving 3D velocity structures in urban areas, where other standard geophysical methods might fail. Including in the analysis the horizontal-component recordings and considering also the amplitude variation with distance of the ground motion will be subjects of future investigations.

Acknowledgements. We are grateful to B. Liss, A. Manconi, R. Milkereit, R. Bauz, for the fieldwork. K Fleming kindly improved the English. Some of the figures were generated using GMT [49] thanks to the help of R. Milkereit. Instruments were provided by the Geophysical Instrumental Pool, Potsdam (GIPP).

REFERENCES

- Aki, K., 1957. Space and time spectra of stationary stochastic waves, with special reference to microtremors, *Bulletin of the Earthquake Research Institute*, 35, 415-456.
- Arai, H. & Tokimatsu, K., 2004. S-wave velocity profiling by inversion of microtremor H/V spectrum, *Bull. Seism. Soc. Am.*, 94, 1, 53-63.
- Ammon, C.J., & Vidale, J.E., 1993. Tomography without rays, *Bull. Seism. Soc. Am.*, 83, 509-528.
- Bakulin, A., & Calvert, R., 2004. Virtual source: new method for imaging and 4D below complex overburden: 74th Annual International Meeting, Society of Exploration Geophysicists, Expanded Abstracts, 2477-2480.
- Bakulin, A., & Calvert, R., 2006. The virtual source method: Theory and case study. *Geophysics*, 71, no. 4, S1139-S1150.
- Bensen, G.D., Barmin, M.P., Levshin, A.L., Lin, F., Moschetti, M.P., Shapiro, N.M., Yang, Y., & Ritzwoller, M.H., 2007. Processing ambient noise seismic data to obtain reliable broadband surface wave dispersion measurements, *Geophys. J. Int* 169, 1239-1260, doi: 10.1111/j.1365-246X.2007.03374.x.
- Brenguier, F., Shapiro, N.M., Campillo, M., Nercessian, A., & Ferrazzini, V., 2007. 3-D surface wave tomography of the Piton de la Fournaise volcano using seismic noise correlations, *Geophysical Research Letters*, 34, L02305, doi:10.1029/2006GL028586.
- Campillo, M., & Paul, A., 2003. Long-range correlations in the seismic coda, *Science* 299, 547-549.
- Capon, J., Greenfield, R.J., & Kolker, R.J., 1967. Multidimensional Maximum-Likelihood Processing of a Large Aperture Seismic Array, *Proceedings of the IEEE*, vol.55, N.2.
- Chávez-García, F. J., & Luzón, F., 2005. On the correlation of seismic microtremors, *J. Geophys. Res.*, 110, B11313, doi:10.1029/2005JB003671
- Chávez-García, F. J., & Rodríguez, M., 2007. The correlation of microtremors: empirical limits and relations between results in frequency and time domains, *Geophys. J. Int.*, 171, 657-664.
- Cho, K. H., Herrmann, R. B., & Ammon, C. J., & Lee, K., 2007. Imaging the Upper Crust of the Korean Peninsula by Surface-Wave Tomography, *Bull. Seism. Soc. Am.*, 97, 198-207, doi: 10.1785/0120060096
- Curtis, A., Gerstoft, P., Sato, H., Snieder, R., & Wapenaar, K., 2006. Seismic interferometry – turning noise into signal, *The Leading Edge*, Vol. 25(9), pp.1082-1092.
- Davis, J.C., 2002. Statistics and Data Analysis in Geology. John Wiley & Sons.
- Dong, S., He, R., & Schuster, G., 2006. Interferometric prediction and leastsquares subtraction of surface waves: 76th Annual International Meeting, SEG, Expanded Abstract, 2783-2786.
- Draganov, D., Wapenaar, K., Mulder, W., Singer, J., & Verdel, A., 2007. Retrieval of reflections from seismic background-noise measurements, *Geophysical Research Letters*, 34, L04305.
- Dziewonski, A., Bloch, S., & Landisman, M., 1969. A technique for the analysis of transient seismic signals. *Bull. Seism. Soc. Am.*, 59, 427-444.
- Efron, B., & Gong, G., 1983. A Leisurely Look at the Bootstrap, the Jackknife, and Cross Validation, *The American Statistician*, 37, 1, 36-48.
- Gerstoft, P., Sabra, K.G., Roux, P., Kuperman, W.A., & Fehler, M.C., 2006. Green's functions extraction and surface-wave tomography from microseisms in southern California, *Geophysics*, 71, 4, 23-32.
- Golub G.H., & Reinsch C., 1970. Singular Value Decomposition and Least Square Solutions. In J. H. Wilkinson and C. Reinsch, editors, *Linear Algebra, volume II of Handbook for Automatic Computations*, chapter I/10, pages 134-151. Springer Verlag.
- Halliday, D.F., Curtis, A., Robertsson, J.O.A., and van Manen, D-J, 2007. Interferometric surface-wave isolation and removal. *Geophysics*, Vol. 72, No 5, A67-A73.

- Halliday, D.F., Curtis, A., & Kragh, E., 2008. Seismic surface waves in a suburban environment – active and passive interferometric methods, *The Leading Edge*, 27,210-218.
- Halliday, D.F., & Curtis, A., 2008. Seismic interferometry, surface waves, and source distribution. In press within *Geophys. J. Int.*
- Halliday, D.F., & Curtis, A., 2008. Seismic interferometry of scattered surface waves in attenuative media. Submitted to
- Kissling, E., 1988. Geotomography with local earthquake data, *Review of Geophysics*, Vol. 25, N. 4, 659-698.
- Kugler, S., Bohlen, T., Forbriger, T., Bussat, S., & Klein, G., 2007. Scholte-wave tomography for shallow-water marine sediments, *Geophys. J. Int.*, 168, 2, 551-570.
- Lai, C.G., 1998. Simultaneous inversion of Rayleigh phase velocity and attenuation for near-surface site characterization. PhD Diss., Georgia Inst. of Techn., Atlanta (Georgia, USA)
- Leveque, J.J., Rivera, L., & Wittlinger, G., 1993. On the use of the checker-board test to assess the resolution of tomographic inversions. *Geophys. J. Int.*, 115, 313-318.
- Li, X.P., Zuehlsdorf, L., & Liebhartdt, G., 1996. Eliminating the effects of the surface weathered layer by using an inverse transfer function, *Scientific Drilling*, 5, 233-242.
- Lin, F-C, Ritwoller, M. H., Townend, J., Bannister, S., & Savage, M. K., 2007. Ambient noise Rayleigh wave tomography of New Zealand, *Geophys. J. Int.*, 170, 649-666, doi: 10.1111/j.1365-246X.2007.03414x.
- Long, L.T., & Kocaoglu, A.H., 2001. Surface-Wave Group-Velocity Tomography for Shallow Structures. *Journal of Environmental and Engineering Geophysics Publications*, 71-81.
- Mehta, K., Snieder, R., & Graizer, V., 2007. Extraction of near-surface properties for a lossy layered medium using the propagator matrix, *Geophys. J. Int.*, 169, 271–280 doi: 10.1111/j.1365-246X.2006.03303.x.
- Metha, K., Bakulin, A., Sheiman, J., Calvert, R., & Snieder, R., 2007. Improving the virtual source method by wavefield separation, *Geophysics*, 72, pp. V79-V86.
- Parolai, S., Spallarossa, D., & Eva, C., 1997. Bootstrap inversion for Pn wave velocity in North-Western Italy, *Annali di Geofisica*, Vol. XL, 133-150.
- Parolai, S., Picozzi, M., Richwalski, S.M., & Milkereit, C., 2005. Joint inversion of phase velocity dispersion and H/V ratio curves from seismic noise recordings using a genetic algorithm, considering higher modes, *Geoph. Res. Lett.*, 32, doi: 10.1029/2004GL021115.
- Parolai, S., Richwalski, S.M., Milkereit, C. & Faeh, D., 2006. S-wave Velocity Profile for Earthquake Engineering Purposes for the Cologne Area (Germany), *Bull Earthq. Eng.*, 65–94, doi:10.1007/s10518-005-5758-2.
- Parolai, S. 2008. Determination of dispersive phase velocities by Complex seismic trace Analysis of Surface Wave (CASW). *Soil Dyn Earthquake Eng*, doi:10.1016/j.soildyn.2008.05.008.
- Paul, A., Campillo, M., Margerin, L., & Larose, E., 2005. Empirical synthesis of time asymmetrical Green functions from the correlation of coda waves, *Journal of Geophysical Research*, V. 110, B08302, doi:10.1029/2004JB003521.
- Pedersen, H.A., Krueger, F. & SVEKALAPKO Seismic Tomography Working Group, 2007. Influence of the seismic noise characteristics on noise correlations in the Baltic shield, *Geophys. J. Int.*, 168, 197–210 doi: 10.1111/j.1365-246X.2006.03177.x
- Picozzi, M., Parolai, S., & Albarello, D., 2005. Statistical Analysis of Noise Horizontal to Vertical Spectral Ratios (HVSr). *Bull. Seism. Soc. Am.*, 95, 1779-1786.
- Picozzi, M., Parolai, S., & Richwalski, S.M., 2005. Joint inversion of H/V ratios and dispersion curves from seismic noise: Estimating the S-wave velocity of bedrock. *Geoph. Res. Lett.*, 32, No.11 doi: 10.1029/2005GL022878.
- Picozzi, M., & Albarello, D., 2007. Combining Genetic and Linearized algorithms for a two-step joint inversion of Rayleigh wave dispersion and H/V spectral ratio curves. *Geophysical Journal International Vol. 169 Issue 1 Page 189 April 2007.*

- Picozzi, M., Strollo, A., Parolai, S., Durukal, E., Özel, O., Karabulut, S., Zschau, J., & Erdik, M., 2007.. Site characterization by seismic noise in Istanbul, Turkey. *doi: 10.1016/j.soildyn.2008.05.007*.
- Sabra, K.G., Gerstoft, P., Roux, P., Kuperman, W.A., & Fehler, M.C., 2005. Surface wave tomography from microseisms in Southern California, *Geophys. Res. Lett.*, 32, L14311, doi:10.1029/2005GL023155.
- Schuster, G.T., 2001. Theory of daylight/interferometric imaging : tutorial : 63rd Meeting, European Association of Geoscientists and Engineers, *Extended Abstracts*, Session :A32.
- Schuster, G.T., Yu, J., Sheng, J., & Rickett, J., 2004. Interferometric/daylight seismic imaging: *Geophysical Journal International*, 157, 838-852.
- Shapiro, N.M., & Singh, S.K., 1999. A systematic error in estimating surface-wave group velocity dispersion curve and a procedure for its correction, *Bull. Seism. Soc. Am.*, 89, 1138-1142.
- Shapiro, N.M., & Campillo, M., 2004. Emergence of broadband Rayleigh waves from correlations of the ambient seismic noise, *Geophys. Res. Lett.*, 31, L07614, doi:10.1029/2004GL019491.
- Shapiro, N.M., Campillo, M., Stehly, L., & Ritzwoller, M., 2005. High resolution surface wave tomography from ambient seismic noise, *Science*, 307, 1615–1618.
- Snieder, R., 2004. Extracting the Green's function from the correlation of coda waves: A derivation based on stationary phase, *Phys. Rev. E*, 69, doi:10.1103/PhysRevE.69.046610.
- Snieder, R., & Safak, E., 2006. Extracting the Building Response Using Seismic Interferometry: Theory and Application to the Millikan Library in Pasadena, California, *Bull. Seism. Soc. Am.*, 96, 2, 586-598.
- Stehly, L., Campillo, M., & Shapiro, N. M., 2006. A study of the seismic noise from its long-range correlation properties, *J. Geophys. Res.*, B10306, doi:10.1029/2005JB004237
- Tokimatsu, K., Tamura, S., and Kojima, H., 1992. Effects of multiple modes on Rayleigh wave dispersion characteristics. *J. Geotech. Eng.*, 118, 1529-1543.
- Tokimatsu, K., 1997. Geotechnical site characterization using surface waves. Earthquake Geotechnical Engineering, Ishihara (ed.), Balkema, Rotterdam, 1333-1368.
- Tukey, J. E., 1974. Introduction to today's data analysis, *Proc. of the Conference on Critical Evaluation of Chemical and Physical Structural Information*, D. R. Lide, Jr., and M. A. Paul (Editors), National Academy of Sciences, Washington, D.C., 3–14.
- Wapenaar, K., 2004. Retrieving the elastodynamic Green's function of an arbitrary inhomogeneous medium by cross correlation, *Phys. Rev. Lett.* 93, 254301.
- Wapenaar, K. & J. Fokkema, 2006. Green's function representations for seismic interferometry, *Geophyscis*, 71, SI33-SI44.
- Weaver, R.L., & Lobkis, O.I., 2001. Ultrasonics without a source: Thermal fluctuation correlation at MHz frequencies, *Phys. Rev. Lett.* 87, 134301–134304.
- Weaver, R. L., & Lobkis, O. I., 2004. Diffuse fields in open systems and the emergence of the Green's function, *J. Acoust. Soc. Am.*, 116, 2731–2734.
- Wiggins, R. A., 1972. The general inverse problem: Implication of surface waves and free oscillations for Earth Structure, *Rev. Geophys.*, 10, 251–285.
- Yamanaka, H. & Ishida, H., 1996. Application of Generic algorithms to an inversion of surface-wave dispersion data, *Bull. Seism. Soc. Am.*, 86, 436-444.
- Yang, Y., Ritzwoller, M. H., Levshin, A. L. & Shapiro, N. M. 2007. Ambient noise Rayleigh wave tomography across Europe, *Geophys. J. Int.*, 168, 259–274, doi: 10.1111/j.1365-246X.2006.03203.x.
- Yang, Y., & Ritzwoller, M.H., 2008. Characteristics of ambient seismic noise as a source for surface wave tomography, *Geochemistry Geophysics Geosystems*, Vol. 9, N. 2, doi:10.1029/2007GC001814

- Yaramanci, U., Lange, G., & Hertrich, M., 2002. Aquifer characterisation using Surface NMR jointly with other geophysical techniques at the Nauen/Berlin test site, *Journal of Applied Geophysics*, 50, 47-65.
- Yao, H., van der Hilst, R.D., & De Hoop, M.V., 2006. Surface-wave array tomography in SE Tibet from ambient seismic noise and two station analysis: I—Phase velocity maps, *Geophys. J. Int.*, 166, 732–744.
- Yokoi, T., & Margaryan, S., 2008. Consistency of the spatial autocorrelation method with seismic interferometry and its consequence, *Geophysical Prospecting*, 56, 435-451.

Figure Captions

Figure 1: *a)* Nauen test site, showing the location of the EDL + 4.5Hz sensors (white dots), EDL + 1Hz Mark sensor (white square), EDL + broadband sensors (black dots), and Reftek + 4.5Hz sensors (grey dots), as well as the DC geoelectric and GP radar profiles (dotted line). – *b)* DC geoelectric profile. *c)* GP radar profile (*courtesy of the Department of Applied Geophysics, Technische Universität (TU) Berlin*).

Figure 2: Stability (RMS - root mean square) of the estimated Green's function with respect to the number of stacked windows for 14 Hz and 6 Hz.

Figure 3: Vertical (*a)* and Horizontal (*b)*) components of the Green's functions for a frequency of 6 Hz. The time window selected for estimating the group velocity is indicated by the white background. *c)* Particle motion in the selected time window of *a)* and *b)*.

Figure 4: –*a)* Normalized cross-correlations computed for 14 Hz. *b)*– 2D-wavenumber plot showing the distribution of the noise sources as determined by F-K analysis results for 14 Hz. *c)* Time delays as a function of distance between each pair of stations and orientation of the pair with respect to north. The delay time is indicated by the colour of the symbol.

Figure 5: Same as Figure (4) but for 6 Hz.

Figure 6: Observed (black dots) and theoretical (grey dots) travel times for frequencies 14 Hz and 6 Hz.

Figure 7: Examples of M matrix normalized weights for cells (*bold number*) located at the corner (*a)*), the inner part (*b)*), and along the model edges (*c)*) and the surrounding cells (*italic numbers*).

Figure 8: Inversion results. *a)* Frequency 14 Hz. *b)* Frequency 6 Hz. The images were obtained after 50 and 100 iterations, respectively. Locations of the DC geoelectric and GP radar profiles (green dotted line), and the field track (grey dotted line) are also shown.

Figure 9: *a)* Input models for the validation tests. *b)* Inversion results for the checker-board model. *c)* Inversion results for the Nauen test site structure.

Figure 10: Standard deviation of velocity computed after 1000 repeated bootstrap inversions. *a)* Frequency 14 Hz. *b)* Frequency 6 Hz.

Figure 11: S-wave velocity section extending south west to north east in the centre of the study area along the same DC geoelectric and GP radar profiles.

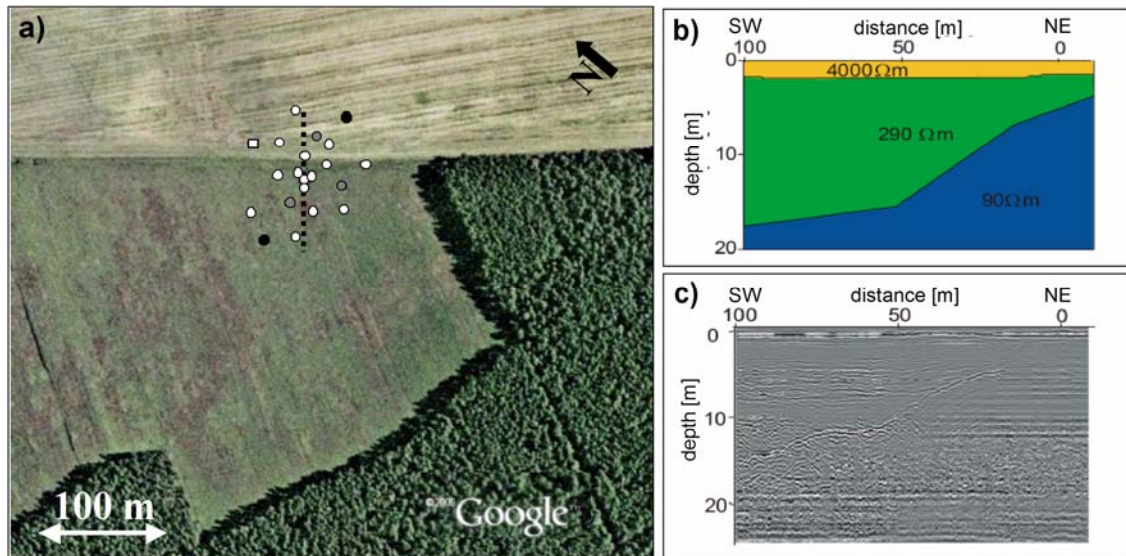


Figure 1: *a)* Nauen test site, showing the location of the EDL + 4.5Hz sensors (white dots), EDL + 1Hz Mark sensor (white square), EDL + broadband sensors (black dots), and Reftek + 4.5Hz sensors (grey dots), as well as the DC geoelectric and GP radar profiles (dotted line). *-b)* DC geoelectric profile. *c)* GP radar profile (courtesy of the Department of Applied Geophysics, Technische Universität (TU) Berlin).

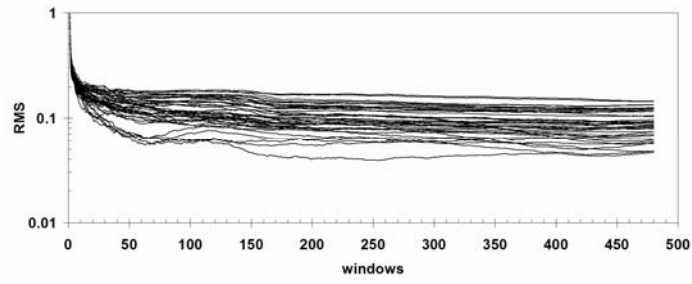


Figure 2: Stability (RMS - root mean square) of the estimated Green's functions with respect to the number of stacked windows for 14 Hz and 6 Hz.

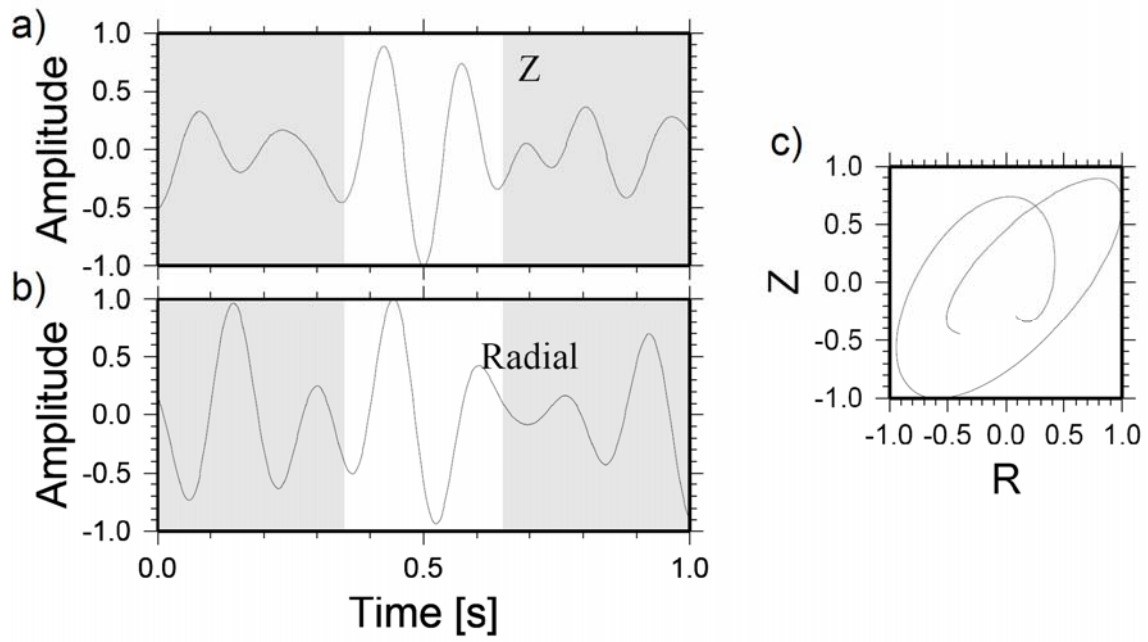


Figure 3: Vertical (*a*) and Radial (*b*) components of the Green's functions for a frequency of 6 Hz. The time window selected for estimating the group velocity is indicated by the white background. *c*) Particle motion in the selected time window of *a*) and *b*).

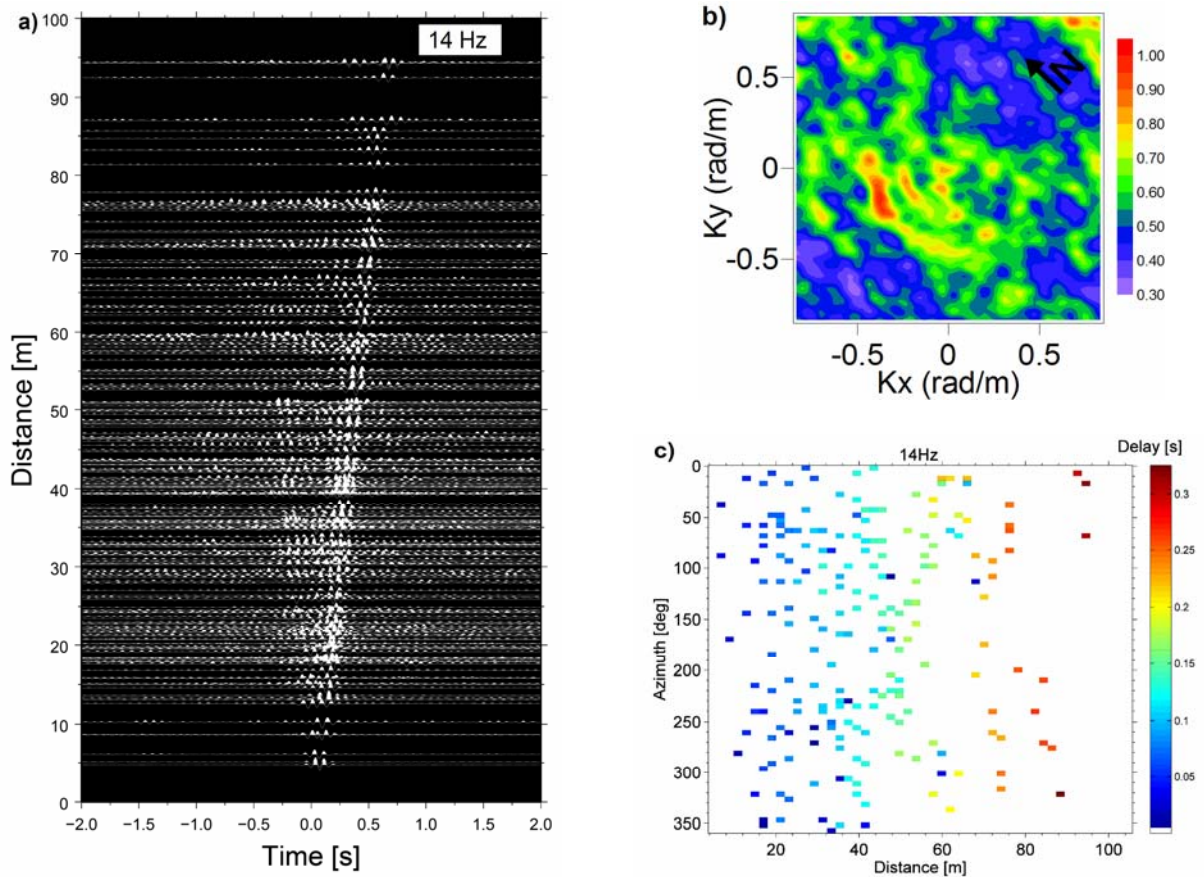


Figure 4: –a) Normalized cross-correlations computed for 14 Hz. b)– 2D-wavenumber plot showing the distribution of the noise sources as determined by F-K analysis results for 14 Hz. c) Time delays as a function of distance between each pair of stations and orientation of the pair with respect to north. The delay time is indicated by the colour of the symbol.

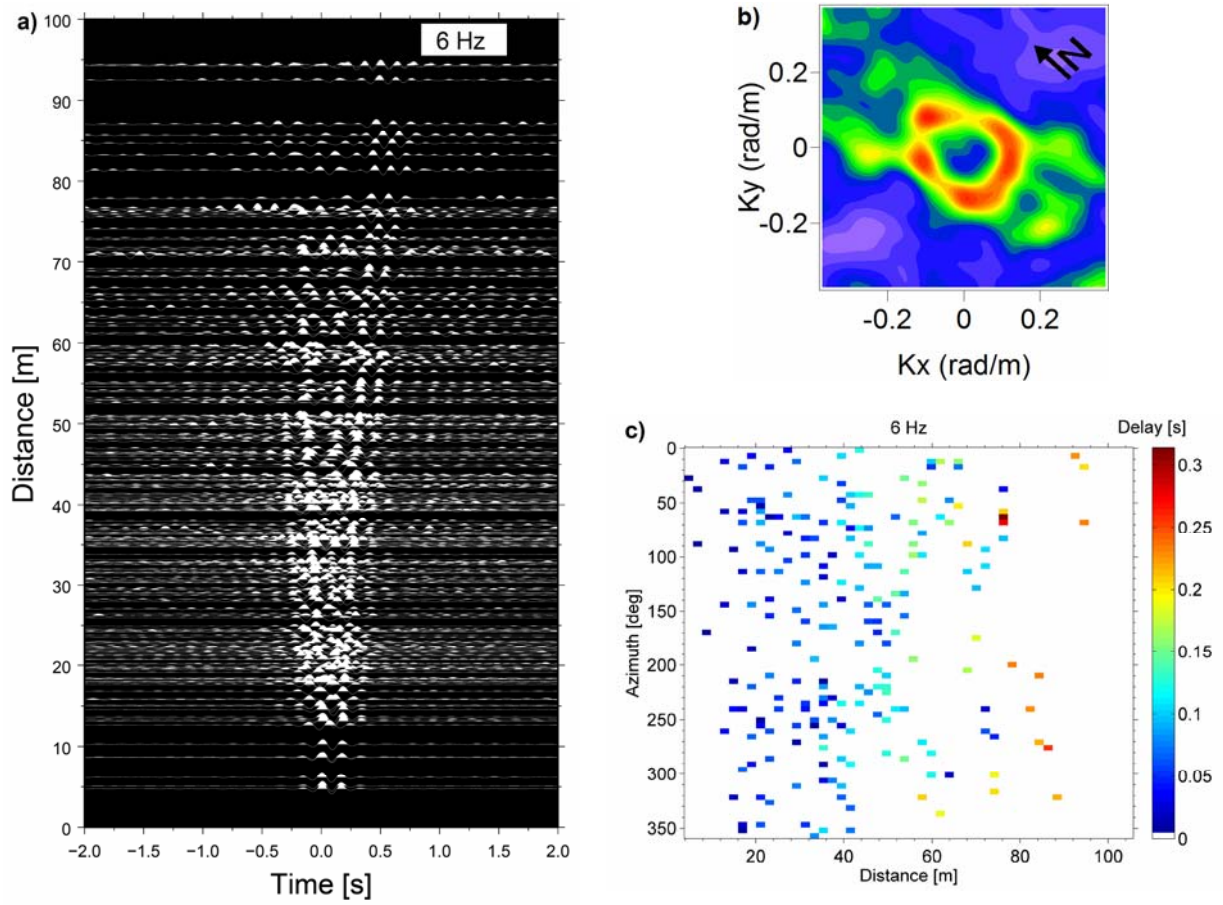


Figure 5: Same as Figure (4) but for 6 Hz.

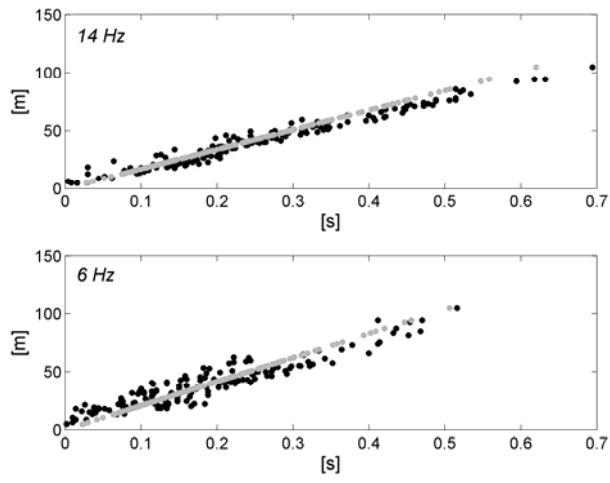


Figure 6: Observed (black dots) and theoretical (grey dots) travel times for frequencies 14 Hz and 6 Hz.

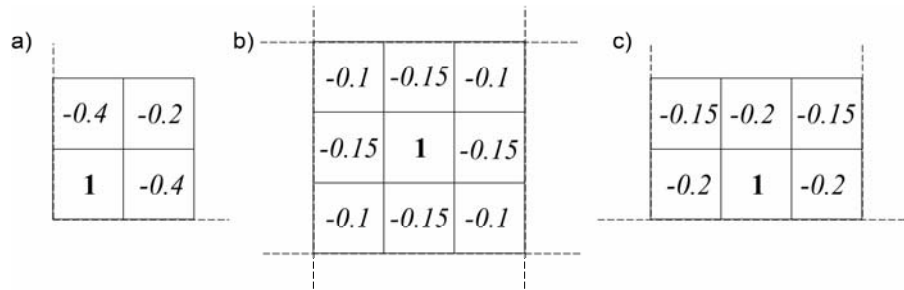


Figure 7: Examples of M matrix normalized weights for cells (*bold number*) located at the corner (a), the inner part (b), and along the model edges (c) and the surrounding cells (*italic numbers*).

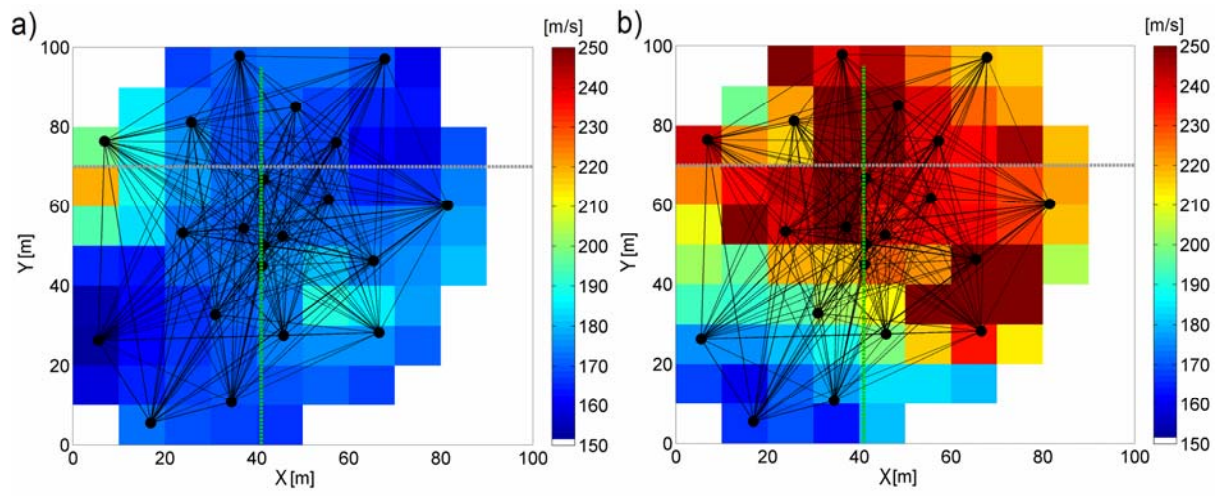


Figure 8: Inversion results. *a)* Frequency 14 Hz. *b)* Frequency 6 Hz. The images were obtained after 50 and 100 iterations, respectively. Locations of the DC geoelectric and GP radar profiles (green dotted line), and the field track (grey dotted line) are also shown.

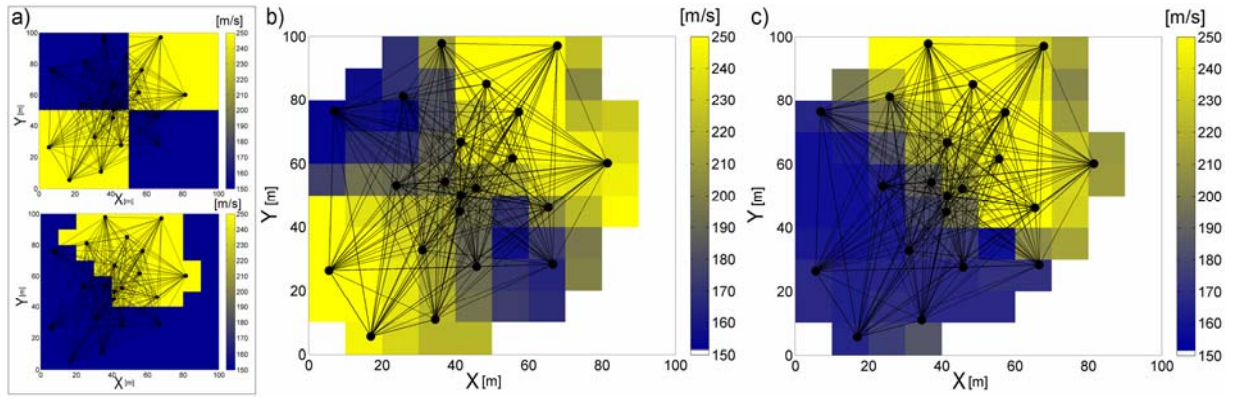


Figure 9: a) Input models for the validation tests. b) Inversion results for the checker-board model. c) Inversion results for the Nauen test site structure.

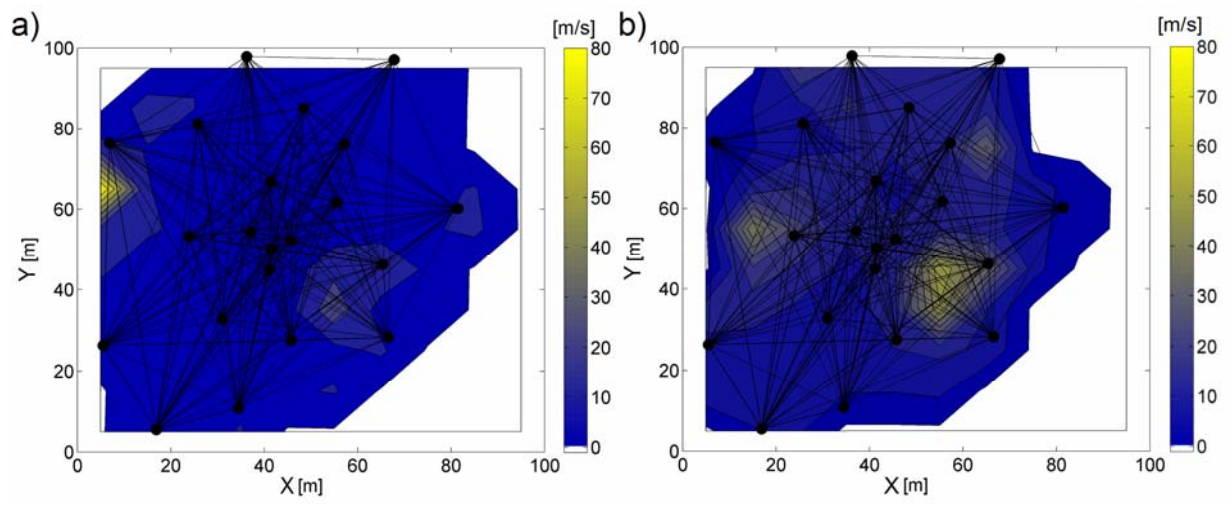


Figure 10: Standard deviation of velocity computed after 1000 repeated bootstrap inversions. *a)* Frequency 14 Hz. *b)* Frequency 6 Hz.

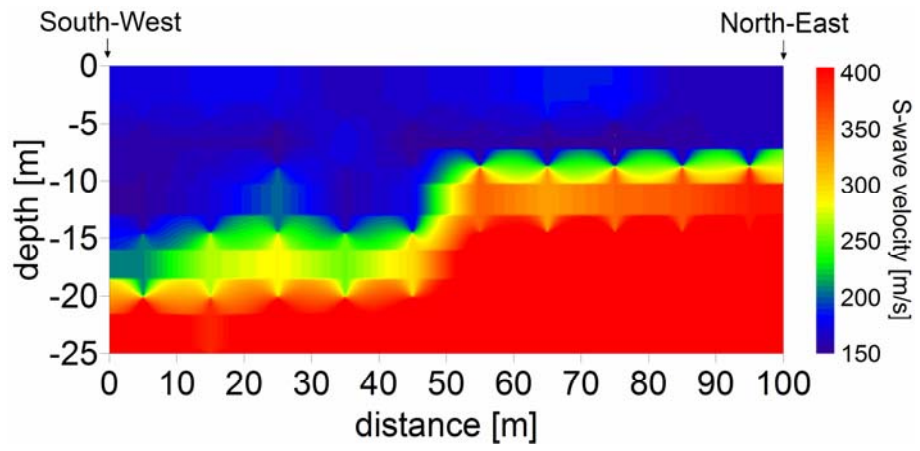


Figure 11: S-wave velocity section extending south west to north east in the centre of the study area along the same DC geoelectric and GP radar profiles.